Published in final edited form as:
Nat Nanotechnol. ; 7(6): 401–407. doi:10.1038/nnano.2012.82.

Quantification of the affinities and kinetics of protein interactions using silicon nanowire biosensors

Xuexin Duan[1], **Yue Li**[2], **Nitin K. Rajan**[3], **David A. Routenberg**[1], **Yorgo Modis**[2], and **Mark A. Reed**[1,3,*]

[1]Department of Electrical Engineering, Yale University, New Haven, Connecticut 06520, USA

[2]Department of Molecular Biophysics and Biochemistry, Yale University, New Haven, Connecticut 06520, USA

[3]Department of Applied Physics, Yale University, New Haven, Connecticut 06520, USA.

Abstract

Monitoring the binding affinities and kinetics of protein interactions is important in clinical diagnostics and drug development because such information is used to identify new therapeutic candidates. Surface plasmon resonance is at present the standard method used for such analysis, but this is limited by low sensitivity and low-throughput analysis. Here, we show that silicon nanowire field-effect transistors can be used as biosensors to measure protein–ligand binding affinities and kinetics with sensitivities down to femtomolar concentrations. Based on this sensing mechanism, we develop an analytical model to calibrate the sensor response and quantify the molecular binding affinities of two representative protein–ligand binding pairs. The rate constant of the association and dissociation of the protein–ligand pair is determined by monitoring the reaction kinetics, demonstrating that silicon nanowire field-effect transistors can be readily used as high-throughput biosensors to quantify protein interactions.

Understanding proteins interactions is key to unravelling their roles in cellular function. Information about these interactions improves our understanding of diseases and can provide the basis for new therapeutic protocols[1]. Affinity biosensors have been developed to analyse ligand–protein or protein–protein interactions, such as those found when antibodies or DNA selectively bind to their corresponding analyte to form a complex. A real-time transduction of this interaction by a sensor device gives detailed information on binding affinities[2] and offers a useful tool for disease diagnosis[3], genetic screening[4] and drug discovery[5]. At present, the most successful surface-based affinity biosensor is surface plasmon resonance[6]. However, surface plasmon resonance has a detection limit for small molecular weights

* Correspondence and requests for materials should be addressed to M.A.R. mark.reed@yale.edu.

Author contributions

X.D. and M.A.R. conceived and designed the experiments. X.D. performed the experiments. X.D. and N.K.R. analysed the data. N.K.R. and D.A.R. fabricated the nanowire devices. Y.L. and Y.M. contributed the DNA and proteins, and X.D. and M.A.R. co-wrote the paper.

Additional information

The authors declare no competing financial interests. Supplementary information accompanies this paper at www.nature.com/naturenanotechnology.

(typically less than 2,000 g mol^{-1}) and also requires integration with optical components, significantly increasing the cost of operation and causing difficulties in carrying out high-throughput analyses. In contrast, silicon nanowires configured as field-effect transistors (Si-NW FETs) can directly translate the analyte–surface interaction into an electrical signal to provide real-time ultrasensitive high-throughput detection of the desired biomolecules, without the requirement for any labels[7,8]. In the past decade, Si-NW FET biosensors have been used to detect a variety of biomolecular interactions with sensitivities below picomolar concentrations[9,10]. However, most of this research has been focused on reducing the detection limit, with little effort expended on quantifying the response— specifically the binding affinities[11,12] and kinetic data[13,14]—of these interactions.

Here, we show that Si-NW FETs can be used as affinity biosensors to effectively determine the affinities and kinetics of two representative protein–receptor binding pairs: (i) the high mobility group box 1 (HMGB1) proteins and DNA and (ii) biotin and streptavidin. The components of the HMGB1–DNA pair have a relatively low affinity for one another and demonstrate slow association/dissociation kinetics[15,16], whereas the biotin– streptavidin pair is known to be the strongest binding pair and has very fast association kinetics[17]. We show that by monitoring the kinetics in real time, the on/off rate constants and equilibrium binding constant for protein–receptor interactions can be determined.

Device calibration and analytical models

To account for sensor variations (including surface functionalization[18]), a calibration scheme must be developed to compare the sensing results across devices. In this work, we used device solution transconductance ($g_m = (\partial I_{ds})/(\partial V_{g,sol})|_{Vds}$) to normalize the sensor responses[19,20]. This calibration was combined with Langmuir isotherms to form an analytical model (equation (1)) that could be used to determine the molecular binding affinities[21]. The device threshold voltage shift ΔV_T can be expressed as

$$\frac{\Delta I_{ds}}{g_m} = \Delta V_T = \frac{q_A}{C_0}[B]_{max} \times \frac{[A]}{[A]+K_D} \quad (1)$$

where q_A is the electric charge contributed by the adsorbed analytes, K_D is the equilibrium (dissociation) constant, C_0 is the analyte/channel capacitive coupling, and $[A]$ and $[B]_{max}$ represent the concentrations of analytes in bulk solution and the maximum surface density of functional binding sites on the Si-NW, respectively (Fig. 1a). The g_m of the device can be determined easily by measuring the I_{ds}–V_g characteristics for each device without performing actual sensing experiments ($g_m = \partial I_d/\partial V_g$). Thus, $\Delta I_{ds}/g_m$ is no longer a function of the device performance, and depends only on the number of molecules adsorbed, as described by the Langmuir isotherm. From equation (1) it can be seen that $(q_A/C_0)[B]_{max}$ and K_D represent the maximum sensor response and affinity properties of the biomolecule interactions, and that both can be derived through sensing measurements for a series of analyte concentrations $[A]$.

Because these sensors give real-time data, both binding constants and rate constants can be determined from the same data set (Fig. 1b). A transport-reaction, two-compartment model (Supplementary Fig. S1) was used to analyse the kinetic data[22,23]:

$$V\frac{\mathrm{d}[A]_{\mathrm{s}}}{\mathrm{d}t}=S\left(k_{\mathrm{M}}\left([A]-[A]_{\mathrm{s}}\right)-k_1[A]_{\mathrm{s}}\left([B]_{max}-[AB]\right)+k_{-1}[AB]\right) \quad (2a)$$

$$\frac{\mathrm{d}[AB]}{\mathrm{d}t}=k_1[A]_{\mathrm{s}}\left([B]_{max}-[AB]\right)-k_{-1}[AB] \quad (2b)$$

$$\frac{\mathrm{d}I}{\mathrm{d}t}=\frac{q_{\mathrm{A}}}{C_0}[AB] \quad (2c)$$

where [*A*] and $[A]_{\mathrm{s}}$ represent the analyte bulk and surface concentration, [*AB*] is the surface density of adsorbed analyte molecules, *V* is the volume of the inner compartment (reaction zone), S is the area of the sensor, and k_1, k_{-1} and k_M are the association, dissociation and effective transport rate constants, respectively. These can be determined by fitting the temporal binding curve with the kinetic model. In practice, differential equations (2a–c) can be simplified under certain conditions to obtain analytical solutions or can be solved by numerical integration.

Si-NW FET biosensor set-up

Figure 1a shows the Si-NW FET biosensor set-up, in which the sensing element is a functionalized silicon 'nanoribbon' with a solution gate (variable voltage for device characterization and fixed voltage to set the operating point while performing sensing measurements), which has been shown to have a sensitivity approaching that of a one-dimensional Si-NW, extending into the femtomolar range for the detection of biotin–streptavidin binding[24]. However, most biomolecular interactions of interest have a lower affinity than the biotin–streptavidin system. To obtain kinetic data within an acceptable time, a higher concentration of analyte is normally desired (because low concentrations of analyte—less than picomolar—may take hours to days)[25]. In such cases, the absolute amount of analyte is always greater than the available binding sites on the sensor surface. Additionally, to obtain real binding kinetics, a fast mixing rate is optimal to reduce the influence of mass transport.

To maximize the sensor response, the buffer ionic concentration should be adjusted to ensure that the absorbed analyte is well within the Debye screening length[26,27]. In our sensing measurements, diluted organic buffers with low ionic strength (1 mM HEPES, pH 7.4, $\lambda_{\mathrm{debye}} \approx 10$ nm) were used.

HMGB1–DNA binding

To validate our Si-NW based affinity biosensor we considered the protein–ligand binding pair HMGB1–DNA. HMGB1 is an abundant vertebrate nuclear protein that binds preferentially to distorted DNA[28,29]. Previous studies have demonstrated that HMGB1–DNA binding has typical dissociation constants (K_D) in the range 10^{-7}–10^{-8} M (refs 30,31). HMGB1 can be covalently bound as a ligand through amine coupling onto isothiocyanatefunctionalized Si-NWs. The positively charged HMGB1 coupling to the Si-

NW can be monitored by the device response, and we found that 10 min incubation time was sufficient for immobilization (Supplementary Fig. S4).

After HMGB1 immobilization, different concentrations of DNA were used to bind with the HMGB1. Between each binding–unbinding cycle, NaCl solution was injected to completely disrupt the HMGB1–DNA complex and regenerate the sensor surface[32].

Figure 2a shows a typical static I_{ds}–V_g curve from the HMGB1-immobilized Si-NW FET before and after exposure to a solution of 300 nM DNA. We calculated the transconductance, g_m, by linear fitting of the *I*–*V* curve and found the change in g_m to be very small (<3%), and the change in the I_{ds}–V_g characteristics after DNA binding could be described as a parallel (threshold voltage) shift of ~202 mV. After DNA desorption and NaCl regeneration, I_{ds}–V_g measurements were taken again to make a comparison with the original curve. Again, the change in g_m was very small and the I_{ds}–V_g shifted back, almost to the original state, demonstrating the successful regeneration of the sensor surface and the stability of our devices. These observations were reproduced consistently for a large number of devices. Because g_m can be regarded as a constant within our measuring range, $\Delta I_{ds}/g_m$ can be used to normalize the sensor response. As a control experiment, the isothiocyanate-functionalized sensor without HMGB1 immobilization was used to attempt the detection of DNA under the same conditions; little to no interaction was observed, indicating an absence of non-specific binding (Supplementary Fig. S5)

To determine the binding affinity, sensor responses from different concentrations of DNA were analysed. Figure 2b shows the sensor responses from five different devices with respect to DNA concentration. The measured ΔI_{ds} has been normalized by $\Delta I_{ds}/g_m$. The sensor response shows consistent behaviour across the different devices, and $\Delta I_{ds}/g_m$ increases with increasing concentration of DNA. The data were fit to equation (1) (solid line in Fig. 2b). From this fitting, we obtained the average K_D of the HMGB1–DNA binding as 105±6 nM. (The fit also gives the maximum sensor response, $(q_A/C_0)[B]_{max}$ (¼ ΔV_{Tmax}), which is ~290 mV.)

Figure 2c presents the real-time sensor responses of nine different concentrations of DNA (to HMGB1). The measured current I_{ds} was normalized by subtracting the original current before DNA exposure (I_0) and dividing by g_m. 'Time = 0' is defined as the onset of DNA addition for this and all subsequent figures. The operation time for each step was adjusted at each concentration to achieve an equilibrium state. We observed that increasing the DNA concentration from 3 to 500 nM increased the association rates. However, the dissociation rate appeared to stay the same. A long dissociation time is needed (>2,000 s), so the DNA–HMGB1 binding is rather slow. We also compared different flow speeds (from 20 to 200 ml min^{-1}), but the sensor responses did not show obvious differences, indicating no mass transportation limitations. In this case, a fast mixing model can be used to simplify the two-compartment model, so equations (2a–c) can be solved analytically as first-order absorption (equation (3a)) and desorption (equation (3b)):

$$\frac{I_{ds}(t)}{g_m} = V_{eq}\left(1 - e^{-(k_1[A]+k_{-1})t}\right) \quad (3a)$$

$$\frac{I_{ds}(t)}{g_{\mathrm{m}}} = V_{eq} e^{-k_{-1}t} + V_{\mathrm{r}} \quad (3b)$$

Here, $V_{eq} = (q_A/C_0)(k_1[B]_{max}[A])/(k_1[A] + k_{-1})$ and V_r represents small populations of bound molecule residues after analyte desorption. Equation (3) can be used to fit the real-time sensor responses of HMGB1–DNA binding. The dashed lines in Fig. 2c represent the fits. Both the association and dissociation phases can be fit well by monoexponential curves. The dissociation rate constant k_{-1} was directly determined by fitting only the dissociation phase. The average of k_{-1} was 1.59±0.06 × 10^{-3} s^{-1}. By fitting the association phase, the nine obtained values of ($k_1[A]$ k_{-1}) were then re-plotted versus DNA concentration (Fig. 2d). The slope of the line gives the association rate constant, with k_1 = 1.55±0.02 × 10^5 M^{-1} s^{-1} (R^2 = 0.998). The binding equilibrium constant can be calculated again using $K_{Dcalc} = k_{-1}/k_1$ = 103 nM, which is very close to our affinity analysis (K_D = 105 nM) and consistent with the literature[15,33]. Differences are probably caused by solution versus surface-bound measurements.

Biotin–streptavidin binding

To demonstrate that kinetic analysis using Si-NW FETs can be extended to a lower range of concentration, we chose the high-affinity biotin–streptavidin system. Biotin binding to streptavidin has been studied in detail, and the dissociation constant of ~1 × 10^{-14} M is widely accepted. However, binding kinetics studies using conventional biosensors (for example, surface plasmon resonance) are not trivial due to the high association rate constant (k_1 > 1 × 10^7 M^{-1} s^{-1}). In contrast to surface plasmon resonance, Si-NW FET sensing does not rely on the mass of the analytes, and kinetic analysis of biotin–streptavidin binding below the picomolar range is obtained in this work.

Biotin was immobilized by a NHS–PEG_4–biotin linker (NHS-biotin, with a 2.9 nm PEG arm) using succinimidyl ester chemistry onto an amine-functionalized Si NW. After biotinylation, streptavidin was allowed to bind with biotin and the sensor responses were recorded. Figure 3a presents $I_{ds}2V_g$ characteristics for 2 nM streptavidin binding with biotin on the Si-NW FET, resulting in a parallel *I–V* curve shift to a lower voltage due to the protein's negative charge at pH 7.4 (pI ≈ 5.6), with DV_T = 320 mV. As a negative control, biotin-blocked streptavidin was also injected under the same conditions and no interaction was detected[10].

The kinetics was investigated in a series of time-lapse measurements for streptavidin solutions ranging in concentration from 200 fM to 2 nM. Owing to the rather slow and incomplete desorption of streptavidin, we used five different devices to measure the streptavidin association kinetics for each concentration. The normalized sensor responses (I_{ds}–I_0)/g_m are plotted versus time in Fig. 3b. The binding kinetics show a consistent increase in the rate of association with higher concentrations of streptavidin. Above the picomolar range, the normalized sensor responses (I_{ds}−I_0)/g_m at equilibrium are approximately the same (~320 mV), suggesting sensor saturation. These results are consistent with the relatively small K_D of streptavidin–biotin. The sensor response at 200 fM

did not saturate within our measurement time (2 h), and the binding is still in the linear regime.

We also observed that the initial binding shows a linear response with time and deviates from an exponential relationship, indicating that the sensor response is limited by mass transport. To minimize this limitation we increased the flow rate to a maximum of 300 μl min^{-1} (higher flow rates become impractical for long measurements, as they would exhaust the supply of the analyte); however, a mass transportation limit is still apparent in the binding curve. This is due to the fast reaction rate of streptavidin– biotin binding; streptavidin consumption at the surface is much faster than the supply from the bulk solution through diffusion and convection. Thus, in this case the analyte surface concentration $[A]_s$ is not equal to the bulk concentration [*A*] during binding, and the simple fast-mixing model is not valid. We therefore fit the binding data with a more general kinetic model (equations (2a–c)) in which a mass transportation rate constant is included. As no analytical solutions are known for equations (2a–c), we solved this by numerical integration. Consistencies of the fits were improved by fitting the binding curves recorded for different concentrations of streptavidin with the same kinetic parameters. The best fitting results are shown in Fig. 3b (dashed lines), with resulting rate constants of $k_1 = 5.50 \pm 0.08 \times 10^8\ M^{-1}\ s^{-1}$ and $k_{-1} = 8.80 \pm 0.06 \times 10^{-5}\ s^{-1}$.

We notice that the fit is insensitive to the dissociation rate constant (k_{-1}) because of its small value. A more precise estimate of k_{-1} can be determined from an independent measurement of the dissociation phase only. However, the measured streptavidin dissociation rate with pure buffer is negligible; this is because desorption is also affected by mass transport, which allows the slowly dissociated streptavidin to rebind the empty biotin sites before they can escape to the solution, and no desorption will therefore be observed.

To overcome this we used a competition desorption method using a high concentration of D-biotin in solution as a competitor during streptavidin desorption[34] (Fig. 4a). After streptavidin association, the sensor was subjected to a flow of D-biotin, and the subsequent unbinding events were measured. Figure 4b presents the kinetics of streptavidin desorption. After 4 h continuous rinsing with D-biotin, only 50% of the streptavidin desorbed, indicative of the slow dissociation of streptavidin–biotin. Because a mass transport limit can be excluded due to the high concentration of D-biotin used, the unbinding curve was fit using equation (3b). Interestingly, this shows a poor fit, with a monoexponential decay function. Instead, the unbinding curve can be fit well by an equation with two exponential terms (Fig. 4b, inset). This is probably a result of the multivalent binding of streptavidin with biotin—there are two biotin binding pockets on each side of the streptavidin, so a more complex binding model has to be considered. A similar bi-exponential fit of streptavidin desorption has also been observed using surface plasmon resonance measurements[34,35]. The small exponent value from the bi-exponential terms represents the slow step of the streptavidin–biotin dissociation, and from the best fit result (Fig. 4b, dashed line), $k_{-1} = 3.10 \pm 0.07 \times 10^{-5}\ s^{-1}$, which is very close to the value obtained from the association phase. Our streptavidin–biotin binding rate constants are in good agreement with previous studies[36,37]. The affinity equilibrium constant of streptavidin– biotin can be calculated by $K_D = k_{-1}/k_1 = 56$ fM.

Discussion and conclusions

One improvement to the binding kinetics studies would be to modify the receptor surface density to minimize the mass transport limit. From equations (2a–c), as the receptor density on the sensor surface is increased, the binding reaction at the sensor surface speeds up and the binding kinetics become more affected by analyte transport. In the other limit, as receptor density is reduced, transport effects decrease and the binding data become strongly dependent on the reaction rate constants. However, this will reduce the sensor response. Research is ongoing to optimize the surface receptor densities and study their effects on binding kinetics. Another consideration is the effect of device geometry on the affinity and kinetics parameters. In this work, we use silicon-nanoribbon-type biosensors; it will be interesting to compare the affinities and kinetics measurements from smaller wires, especially one-dimensional nanowires that have a similar size to the analyte molecules.

We have performed a comprehensive study of Si-NW FET biosensors and successfully demonstrated their use as affinity biosensors in the quantification of protein binding affinities and kinetics. A calibration method has been presented to reduce the device-to-device variation in the sensor response. Based on the sensing mechanism, an analytical model has been developed that provides a precise and clear description of the processes involved in protein–ligand interactions on silicon nanowires. The Si-NW FETs, combined with the analytical model, have successfully analysed binding in both the association and dissociation phases. The resulting binding affinities and rate constants are comparable to the values provided in the literature. These results indicate that the Si-NW FET can be used as a powerful tool for real-time, *in situ* detection of protein adsorption and desorption without labelling, and with sensitivity into the femtomolar range.

The approach presented here can be used broadly in fundamental research of protein–ligand and protein–protein interactions and in quantifying their binding affinities and kinetics. It can also provide a high-throughput tool through the integration of arrays of nanowires within the same chip, which is important in disease diagnosis, genetic screening and drug discovery. We believe that this approach will bring nanoscale FET sensor technology a step closer to commercial applications.

Methods

Si-NW FET biosensor fabrication

The devices were fabricated from 4-inch silicon on insulator (SOI) wafers (Soitec). The silicon active layer (p-type doping, 1×10^{15} cm^{-3}) was thinned to ~45 nm by thermal oxidation and silicon oxide was removed by wet etching (BOE Etch). The source and drain regions, as well as the back-gate, were patterned by contact lithography and doped by BF_2^+ implantation. Following dopant activation in a furnace at 1,000 °C, the nanoribbon mesas were defined by optical lithography and transferred to the active layer (that is, etched into the top silicon layer; Supplementary Fig. S2b) using a Cl_2 inductively coupled plasma etch (Oxford 100). The fabricated silicon wire had a typical active layer thickness of 45 nm, and width and length of 1 μm and 10 μm, respectively. A 20-nm-thick layer of silicon oxide was grown over the wafer using dry oxidation in a chemical vapour deposition (CVD) furnace.

The devices were then metallized by evaporation of titanium/aluminium followed by a lift-off process. A second metallization step was carried out for the solution-gate electrode by evaporating titanium/platinum then patterning by lift-off. The metal contacts were annealed in a rapid thermal processor at 450 °C for 1 min and devices were measured to ensure ohmic contacts. The final step was to passivate the devices with a 1 mm layer of SU8 photoresist with lithographically patterned openings at the top of the devices, contact pads and the solution-gate electrode. The wafer was then hard-baked at 130 °C for 20 min.

Device functionalization

The Si-NW oxide surfaces were cleaned with ultraviolet ozone for 5 min before functionalization. 3-Aminopropyltriethoxysilane (APTS) was then allowed to evaporate onto the SiO_2 surface by gas-phase deposition for 5 h. The devices were then baked in a vacuum oven for 30 min at 120 °C.

General sensing set-up

The functionalized dies were packaged using 16-pin ceramic headers (Spectrum Semiconductor Materials). The fluid delivery system was then mounted on top of the dies. The mixing cells were created by epoxying thin-walled, ~2-mm-diameter polytetrafluoroethylene (PTFE, also known as Teflon) tubing to the chip surface and by inserting thinner tubing (0.5 mm) to serve as the fluid supply and return. Multiplexed *I*–*V* and d.c. time measurements were carried out using a custom-made system with a National Instruments Data Acquisition Card and Keithley 2636 Dual Source Measure Unit. For all measurements, I_{ds} was measured at 0.5 s intervals while V_{ds} and V_g were held constant; V_{ds} was set to 0.1 V and V_g was determined from I_d–V_g measurement before sensing. The active region of all devices used for sensing experiments was 10 μm in length and 1 μm in width. HEPES buffer (1 mM, pH 7.4, ionic strength = 1 mM) was used throughout our experiments. For studies involving analyte addition, ‘time = 0’ was defined as the onset of protein/DNA addition. In all plots the initial sensor equilibration time is not shown.

Analysis cycle

A typical binding cycle observed with our biosensor is shown in Fig. 1b. After receptor immobilization, analyte solution was passed over the receptor. The surface charges induced by analyte binding led to a change in the measured current (I_{ds}). Analysis of this part of the binding curve gave the association rate. After equilibrium, the analyte solution was replaced by buffer and the receptor– analyte complex was allowed to dissociate. Analysis of these data gives the dissociation rate constant for the interaction. After unbinding, a regeneration step was introduced to totally remove the absorbed molecules and regenerate the free receptor on the silicon surface. The entire binding cycle was repeated several times at varying concentrations of analyte to generate a robust data set for affinity and kinetics analysis.

DNA sensing

Transformation of the amino-functionalized device to an isothiocyanate-bearing layer was accomplished by exposure to a 0.01 M solution of 1,4-phenylene diisothiocyanate (PDC) in

ethanol at 40 °C for 1 h, followed by rinsing with copious amounts of ethanol and water. HMGB1 was then immobilized for 30 min in MES buffer (pH 5.6). The sensor was washed with buffer to remove the physically absorbed HMGB1 (Supplementary Fig. S3). DNA solutions were injected at 30 μl min^{-1}. After DNA adsorption and desorption, the sensor was regenerated with 1 M NaCl (5 min) and replaced by buffer before the next injection. To facilitate sensor regeneration, we started with the lowest concentration of DNA (3 nM) and increased it to 500 nM.

Biotin–streptavidin sensing

Sensor surface biotinylation was performed with EZ-Link NHS–PEG_4–biotin at pH 7.4 for 1 h on the amine-functionalized Si-NW. After rinsing with buffer, streptavidin was injected at 300 μl min^{-1} and sensor responses were recorded. For streptavidin desorption, 1 mM D-biotin in HEPES was used with a flow rate of 30 gμl min^{-1}.

Supplementary Material

Refer to Web version on PubMed Central for supplementary material.

Acknowledgments

The authors acknowledge financial support from the Netherlands Organization for Scientific Research (NWO, Rubicon grant), the National Institutes of Health (NIH R01EB008260 and P01GM022778), the Burroughs Welcome Fund (to Y.M.) and DTRA (HDTRA1-10-1-0037). The authors thank A. Vacic, M. Weber and W. Guan for help with the electrical measurement and helpful discussions.

References

1. Boccaletti S, Latora V, Moreno Y, Chavez M, Hwang DU. Complex networks: structure and dynamics. Phys. Rep. 2006; 424:175–308.
2. Wilson GS, Gifford R. Biosensors for real-time *in vivo* measurements. Biosens. Bioelectron. 2005; 20:2388–2403. [PubMed: 15854814]
3. Cheng MMC, et al. Nanotechnologies for biomolecular detection and medical diagnostics. Curr. Opin. Chem. Biol. 2006; 10:11–19. [PubMed: 16418011]
4. D'Orazio P. Biosensors in clinical chemistry. Clin. Chim. Acta. 2003; 334:41–69. [PubMed: 12867275]
5. Arlett JL, Myers EB, Roukes ML. Comparative advantages of mechanical biosensors. Nature Nanotech. 2011; 6:203–215.
6. Cooper MA. Optical biosensors in drug discovery. Nature Rev. Drug Discov. 2002; 1:515–528. [PubMed: 12120258]
7. Curreli M, et al. Real-time, label-free detection of biological entities using nanowire-based FETs. IEEE Trans. Nanotech. 2008; 7:651–667.
8. Stern E, Vacic A, Reed MA. Semiconducting nanowire field-effect transistor biomolecular sensors. IEEE Trans. Electron Dev. 2008; 55:3119–3130.
9. Cui Y, Lieber CM. Functional nanoscale electronic devices assembled using silicon nanowire building blocks. Science. 2001; 291:851–853. [PubMed: 11157160]
10. Stern E, et al. Label-free immunodetection with CMOS-compatible semiconducting nanowires. Nature. 2007; 445:519–522. [PubMed: 17268465]
11. Wang WU, Chen C, Lin KH, Fang Y, Lieber CM. Label-free detection of small-molecule–protein interactions by using nanowire nanosensors. Proc. Natl Acad. Sci. USA. 2005; 102:3208–3212. [PubMed: 15716362]

12. De Vico L, et al. Quantifying signal changes in nano-wire based biosensors. Nanoscale. 2011; 3:706–717. [PubMed: 21173975]
13. Bunimovich YL, et al. Quantitative real-time measurements of DNA hybridization with alkylated nonoxidized silicon nanowires in electrolyte solution. J. Am. Chem. Soc. 2006; 128:16323–16331. [PubMed: 17165787]
14. Squires TM, Messinger RJ, Manalis SR. Making it stick: convection, reaction and diffusion in surface-based biosensors. Nature Biotechnol. 2008; 26:417–426. [PubMed: 18392027]
15. Tian J, et al. Toll-like receptor 9-dependent activation by DNA-containing immune complexes is mediated by HMGB1 and RAGE. Nature Immunol. 2007; 8:487–496. [PubMed: 17417641]
16. Li Y, Berk IC, Modis Y. DNA binding to proteolytically activated TLR9 is sequence-independent and enhanced by DNA curvature. EMBO J. 2012; 31:919–931. [PubMed: 22258621]
17. Wilchek M, Bayer EA. Introduction to avidin-biotin technology. Methods Enzymol. 1990; 184:5–13. [PubMed: 2201884]
18. Balasubramanian K. Challenges in the use of 1D nanostructures for on-chip biosensing and diagnostics: a review. Biosens. Bioelectron. 2011; 26:1195–1204. [PubMed: 20692156]
19. Ishikawa FN, et al. A calibration method for nanowire biosensors to suppress device-to-device variation. ACS Nano. 2009; 3:3969–3976. [PubMed: 19921812]
20. Lee BY, et al. Universal parameters for carbon nanotube network-based sensors: can nanotube sensors be reproducible? ACS Nano. 2011; 5:4373–4379. [PubMed: 21615164]
21. Abe M, et al. Quantitative detection of protein using a top-gate carbon nanotube field effect transistor. J. Phys. Chem. C. 2007; 111:8667–8670.
22. Myszka DG, He X, Dembo M, Morton TA, Goldstein B. Extending the range of rate constants available from BIACORE: interpreting mass transport-influenced binding data. Biophys. J. 1998; 75:583–594. [PubMed: 9675161]
23. Gaster RS, et al. Quantification of protein interactions and solution transport using high-density GMR sensor arrays. Nature Nanotech. 2011; 6:314–320.
24. Elfstroem N, Karlstroem AE, Linnrost J. Silicon nanoribbons for electrical detection of biomolecules. Nano Lett. 2008; 8:945–949. [PubMed: 18266330]
25. Sheehan PE, Whitman LJ. Detection limits for nanoscale biosensors. Nano Lett. 2005; 5:803–807. [PubMed: 15826132]
26. Bergveld P. A critical-evaluation of direct electrical protein-detection methods. Biosens. Bioelectron. 1991; 6:55–72. [PubMed: 2049171]
27. Stern E, et al. Importance of the debye screening length on nanowire field effect transistor sensors. Nano Lett. 2007; 7:3405–3409. [PubMed: 17914853]
28. Bianchi ME, Beltrame M, Paonessa G. Specific recognition of cruciform DNA by nuclear-protein HMG1. Science. 1989; 243:1056–1059. [PubMed: 2922595]
29. Ivanov S, et al. A novel role for HMGB1 in TLR9-mediated inflammatory responses to CpG-DNA. Blood. 2007; 110:1970–1981. [PubMed: 17548579]
30. Ohndorf UM, Rould MA, He Q, Pabo CO, Lippard SJ. Basis for recognition of cisplatin-modified DNA by high-mobility-group proteins. Nature. 1999; 399:708–712. [PubMed: 10385126]
31. Pil PM, Lippard SJ. Specific binding of chromosomal protein-HMG1 to DNA damaged by the anticancer drug cisplatin. Science. 1992; 256:234–237. [PubMed: 1566071]
32. Halford SE, Marko JF. How do site-specific DNA-binding proteins find their targets? Nucleic Acids Res. 2004; 32:3040–3052. [PubMed: 15178741]
33. Jung Y, Lippard SJ. Nature of full-length HMGB1 binding to cisplatin-modified DNA. Biochemistry. 2003; 42:2664–2671. [PubMed: 12614161]
34. Perez-Luna VH, et al. Molecular recognition between genetically engineered streptavidin and surface-bound biotin. J. Am. Chem. Soc. 1999; 121:6469–6478.
35. Jung LS, Nelson KE, Stayton PS, Campbell CT. Binding and dissociation kinetics of wild-type and mutant streptavidins on mixed biotin-containing alkylthiolate monolayers. Langmuir. 2000; 16:9421–9432.
36. Buranda T, et al. Ligand receptor dynamics at streptavidin-coated particle surfaces: a flow cytometric and spectrofluorimetric study. J. Phys. Chem. B. 1999; 103:3399–3410.

37. Tang YJ, Mernaugh R, Zeng XQ. Nonregeneration protocol for surface plasmon resonance: study of high-affinity interaction with high-density biosensors. Anal. Chem. 2006; 78:1841–1848. [PubMed: 16536419]

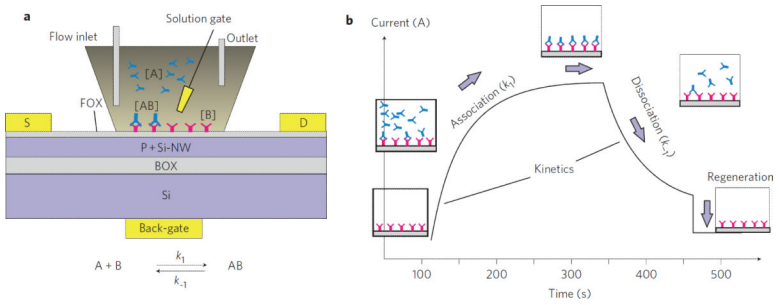

Figure 1. Schematic of the Si-NW FET biosensor set-up and binding cycles

a, Cross-section of the p-doped (P+) Si-NW biosensor set-up showing the source (S) and drain (D). FOX, front oxide (20 nm silicon oxide in direct contact with solutions); BOX, buried oxide (145 nm silicon oxide). A platinum solution gate is used as a reference electrode to bias the Si-NW FETs to the desired operating point, and the back-gate is used as a screening tool for device characterization before solution measurements. The sensing element is a 10-μm-long, 1-μm-wide nanoribbon with a typical active layer thickness of 45 nm (light blue). The fluid delivery system (trapezoidal) with flow inlet and outlet (PTFE tubes) is mounted on top of the chip. The Si-NW is functionalized with amino silanes followed by immobilized receptors [B] (red 'Y' shapes). Analytes [A] (blue 'Y' shapes) are delivered through the PTFE tubes. When the analytes bind to the receptors, the change in conductance in the Si-NWs is detected by the FET. Protein interactions, which are reversible, can be described as a reversed reaction (left bottom) with an association rate constant k_1 and dissociation rate constant k_{-1}. **b**, Typical schematic binding cycle for measurements obtained using the Si-NW FET biosensor. At t = 100 s, a solution of analyte in the flowing buffer is passed over the receptor. As the analyte binds to the surface, the charges of the analytes cause a change in the current signal. Analysis of this part of the binding curve gives the apparent association rate. If the concentration of the analyte is known, then the association rate constant of the interaction (k_1) can be determined. At equilibrium, the amount of analyte associating and dissociating with the receptor is equal. The response level at equilibrium is related to the concentration of active analyte in the sample. At t = 350 s, the analyte solution is replaced by pure buffer and the receptor–analyte complex is allowed to dissociate. Analysis of these data gives the dissociation rate constant k_{-1} for the interaction. Introduction of a regeneration solution (for example, high salt, low pH) is used at t = 460 s to disrupt binding and regenerate the free receptor.

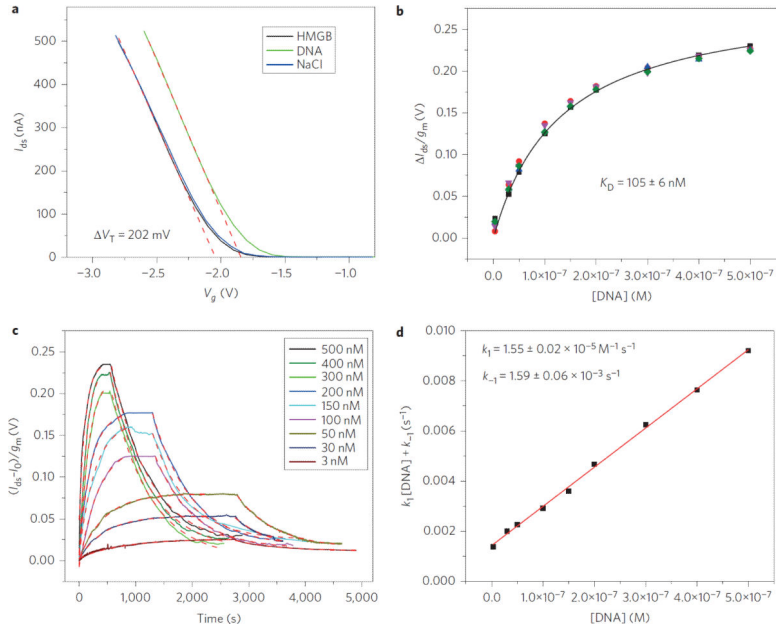

Figure 2. Measurements of HMGB1 and DNA binding using the Si-NW FET

a, I_d2V_g characteristics of HMGB1–DNA binding measured by Si-NW FETs. Black, after HMGB1 immobilization; green, after interaction with 300 nM DNA; blue, after DNA desorption and surface regeneration with 1 M NaCl. Threshold voltage V_T was obtained by linear extrapolation of the *I*–*V* curve to $x = 0$. **b**, Normalized Si-NW sensor responses ($\Delta I_{ds}/g_m$) of HMGB1–DNA interactions as a function of DNA concentration. Five different sets of nanowires are used. The solid line is a fit using equation (1), and K_D is determined by least-squares fitting, giving 105±6 nM. **c**, Real-time sensor responses of HMGB1–DNA binding. Each curve represents the measurement of a different DNA concentration from the same device, and sensor responses are plotted using $(I_{ds}-I_0)/g_m$. Apparent association rates ($k_1[A] + k_{-1}$) were determined by fitting with equation (3a) for each concentration, and dissociation data were fitted by equation (3b) with a best-fit rate constant of k_{-1} = (1.59±0.06) × 10^{-3} s^{-1} Dashed lines represent the fits. **d**, Plot of apparent association rates ($k_1[A] + k_{-1}$) versus DNA concentration. The linear fit of the data gives the association rate constant k_1 = (1.55±0.02) × 10^5 M^{-1} s^{-1}. For all measurements, V_{ds} = 100 mV, flow rate = 30 µl min^{-1}.

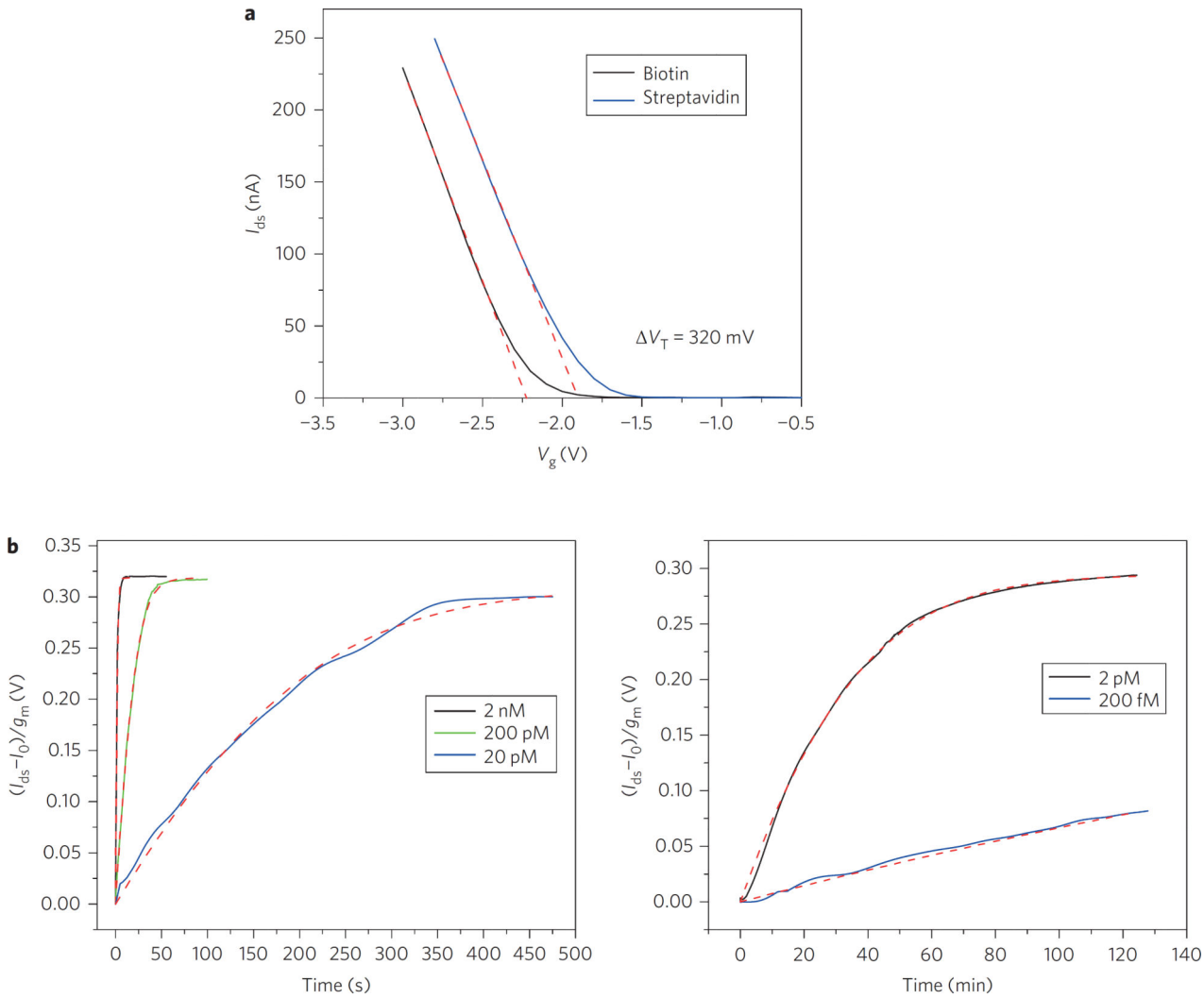

Figure 3. Sensor response of the binding of biotin and streptavidin as measured by the Si-NW FET

a, I_d2V_g characteristics of biotin–streptavidin binding measured by Si-NW FETs. Black, biotin-functionalized Si-NW; blue, after interaction with 2 nM streptavidin. **b**, Real-time sensor responses of biotin–streptavidin binding. Each curve represents measurement from a different device and sensor responses were normalized using $(I_{ds}-I_0)/g_m$. Data were fitted using equations (2a–c), and the rate constants were determined as $k_1 = 5.50\pm0.08 \times 10^8$ M^{-1} s^{-1} and $k_{-1} = 8.80 \pm 0.06 \times 10^{-5}$ s^{-1}. Dashed lines represent the fits. For all measurements, V_{ds} = 100 mV and flow rate = 300μ min_{-1}.

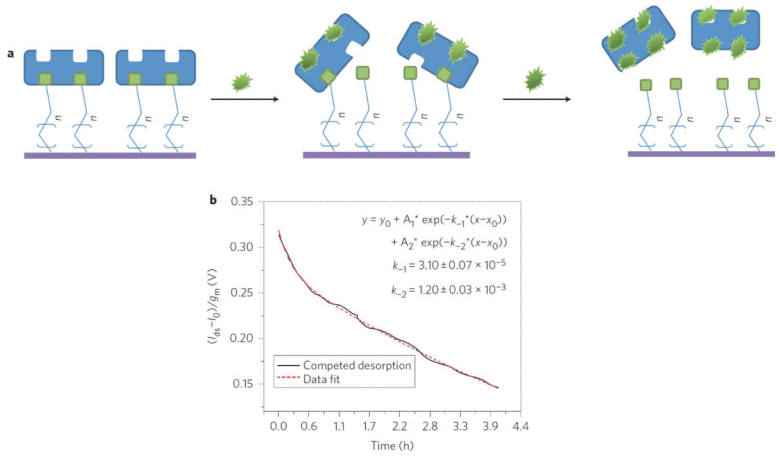

Figure 4. Competitive dissociation processes of streptavidin from a biotin-functionalized surface

a, Schematic of the competitive dissociation processes of streptavidin from the biotin-functionalized surface. Streptavidin (blue) are attached via two biotin-binding sites. Desorption of the complex is achieved by introduction of D-biotin (green), and desorption occurs by sequential dissociation of the streptavidin–biotin bonds. **b**, Sensor response of streptavidin competitive dissociation with D-biotin (solid line), fitted with a bi-exponential decay function (dashed line).